Supporting Information

Facet-Defect Coupling in CuO Catalysts Boosts Ammonia Oxidation Kinetics

Mengyuan Zhao[1], Shaohan Liang[2], Junhui Liang[1,*], Jiahui Hou[1], Jiangchao Lou[1], Xin Yao[3], Huayu Chen[1], Feng Zhou[4,*], Huaizhou Jin[5], Da Chen[1,*]

[1] College of Materials and Chemistry, China Jiliang University, Hangzhou 300018, Zhejiang, China

[2] College of metrology measurement and instrument, China Jiliang University, Hangzhou 300018, Zhejiang, China

[3] College of Optical and Electronic Technology, China Jiliang University, Hangzhou 300018, Zhejiang, China

[4] National Institute of Metrology, Beijing 102200, China

[5] Key Laboratory of Quantum Precision Measurement, College of Physics, Zhejiang University of Technology, Hangzhou, 300018, Zhejiang, China

*Corresponding Author

E-mail: nkljhyx@163.com; zhoufeng@nim.ac.cn; dchen_80@hotmail.com

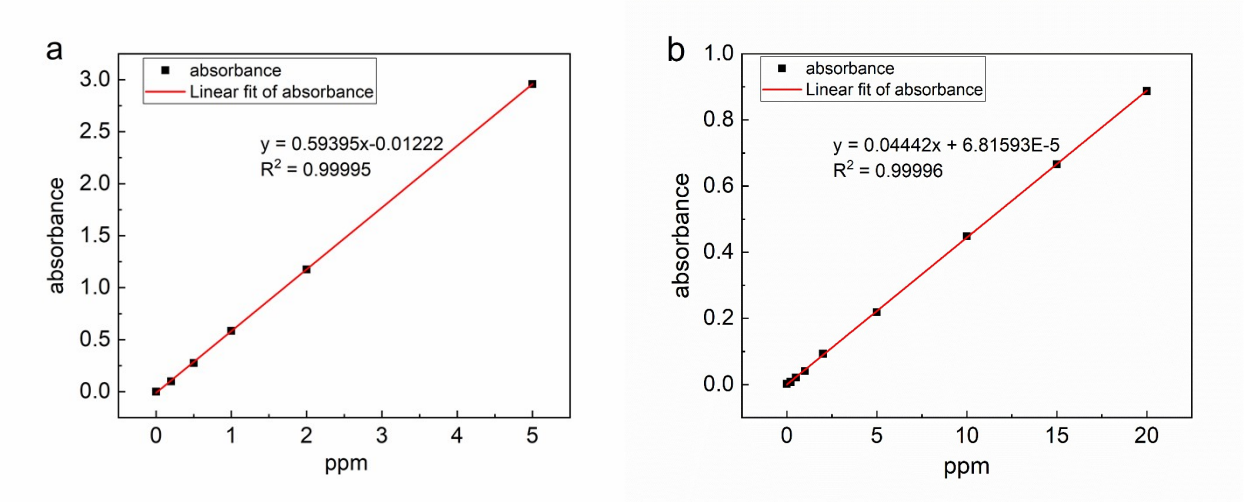

Figure S1. Standard calibration curves for the quantitative analysis of AOR products. (a) Calibration curve for NO_2^- determination using the Griess reagent method, showing absorbance at 540 nm as a function of NO_2^- concentration. (b) Calibration curve for NO_3^- determination using the dual-wavelength direct absorbance method (220 and 275 nm), with corrected UV absorbance plotted against NO_3^- concentration.

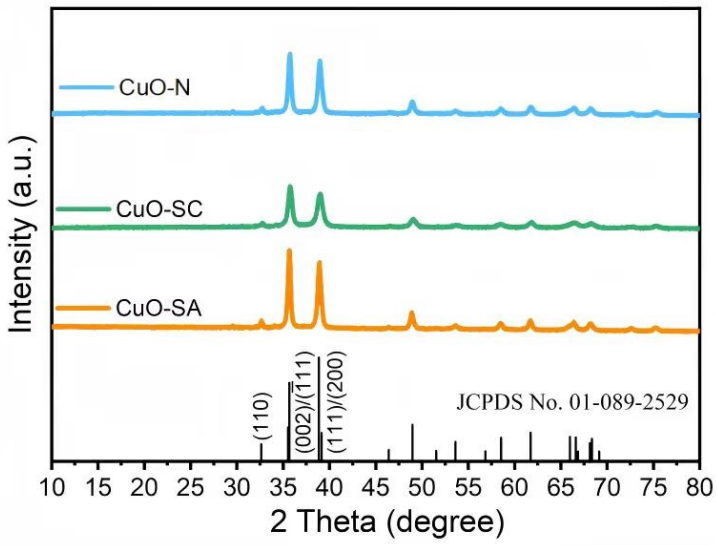

Figure S2. XRD patterns of CuO-N, CuO-SC, and CuO-SA catalysts.

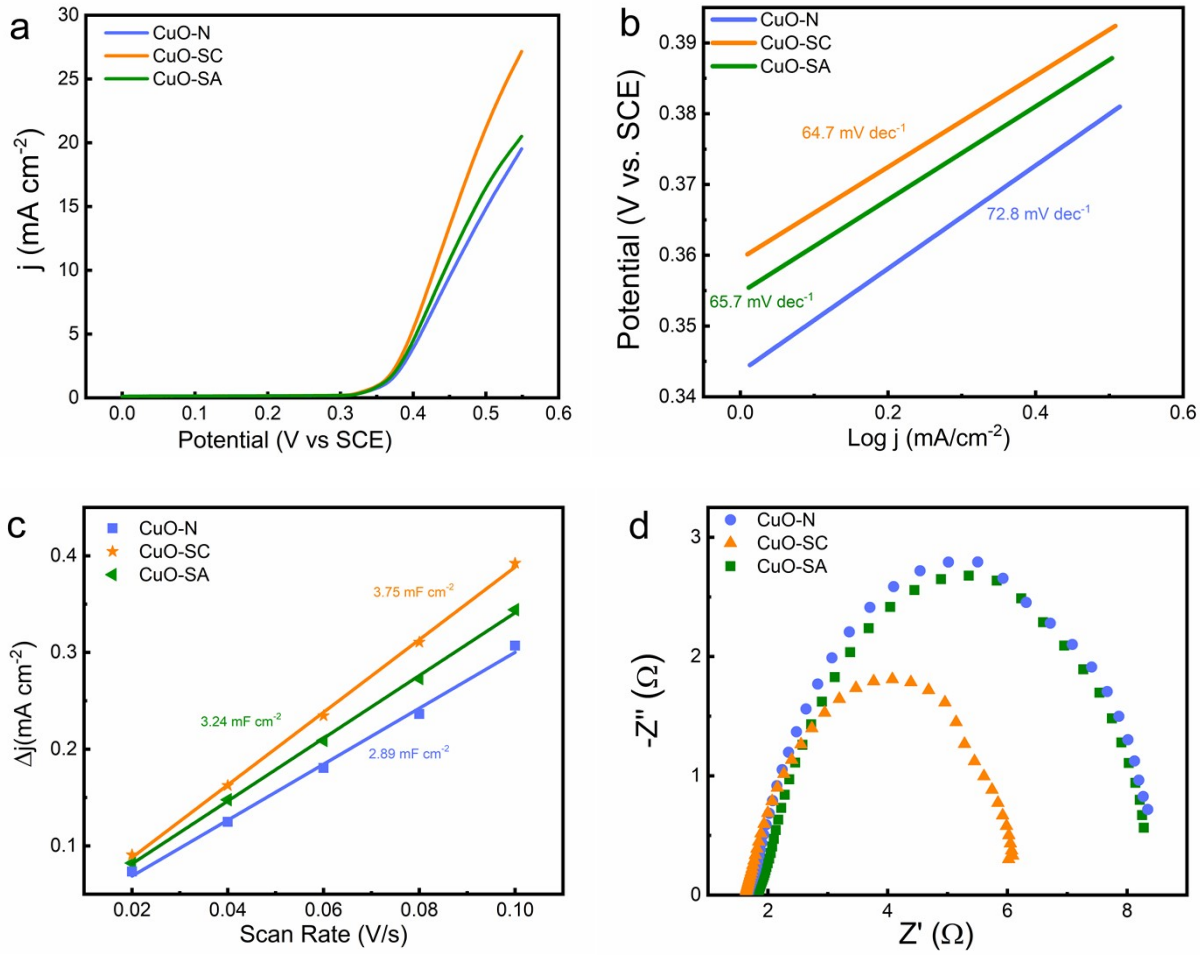

Figure S3. Comparative electrocatalytic performance of CuO catalysts with different exposed facets. (a) LSV curves. (b) Corresponding Tafel slopes. (c) C_{dl} derived from CV scans in the non-Faradaic region. (d) EIS Nyquist plots.

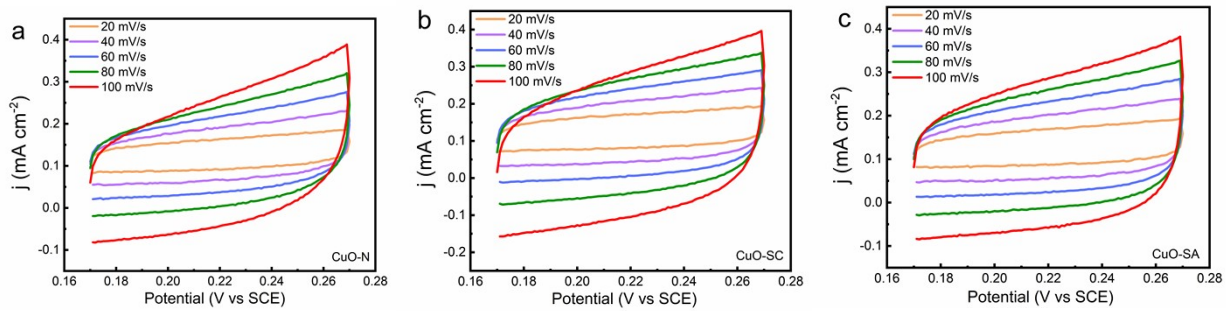

Figure S4. CV curves recorded in the non-Faradaic potential region at various scan rates (20 - 100 mV s^{-1}) for (a) CuO-N, (b) CuO-SC, and (c) CuO-SA

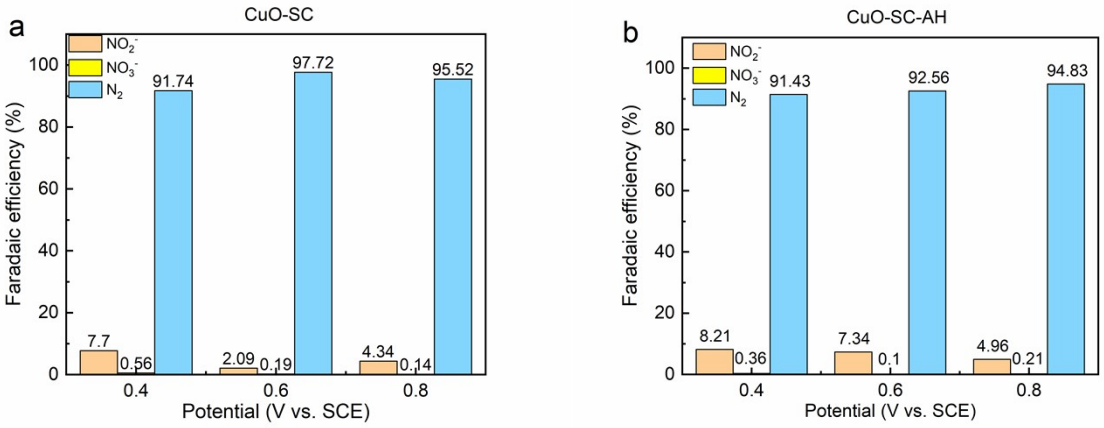

Figure S5. Potential-dependent Faradaic efficiencies (FEs) of AOR products over different catalysts. (a) CuO-SC, and (b) CuO-SC-AH.

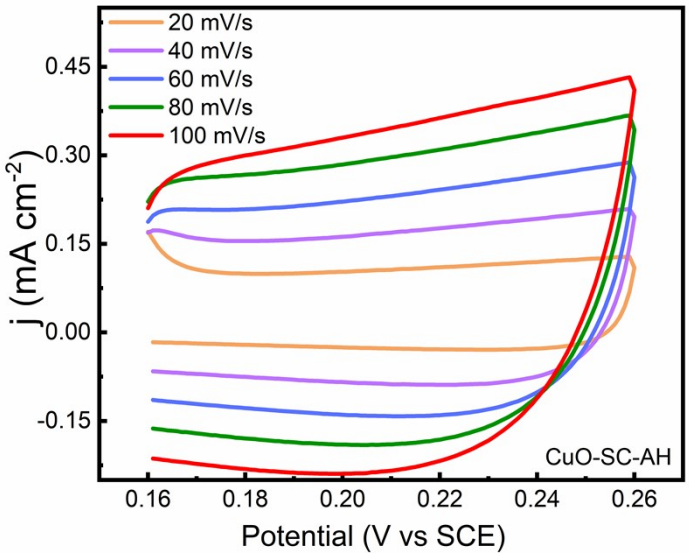

Figure S6. CV curves for CuO-SC-AH recorded in the non-Faradaic potential region at various scan rates (20 - 100 mV s^{-1}).

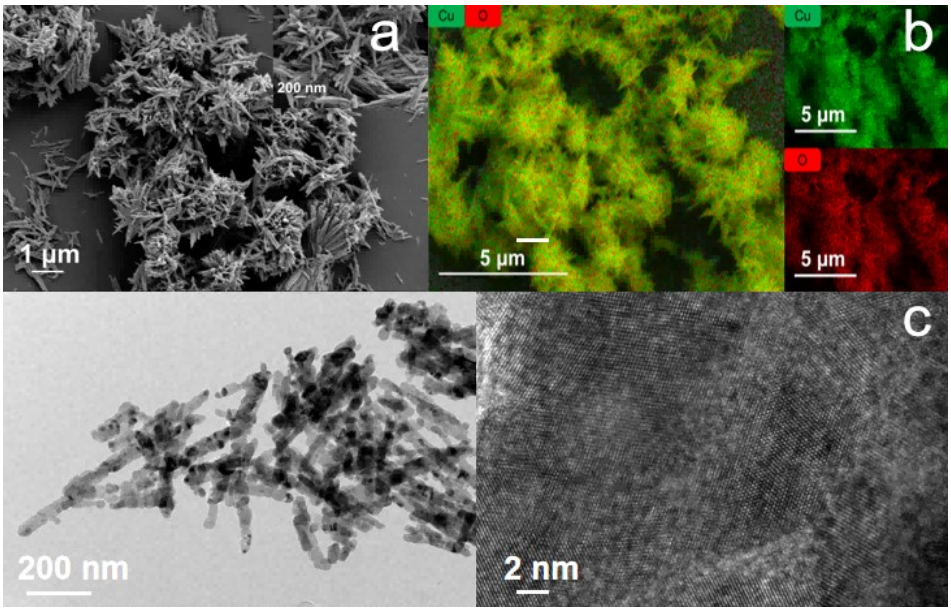

Figure S7. Microstructural and elemental characterization of CuO-SC-AH catalyst. (a) SEM image, (b) Corresponding EDS elemental mapping for Cu and O, and (c)TEM image.

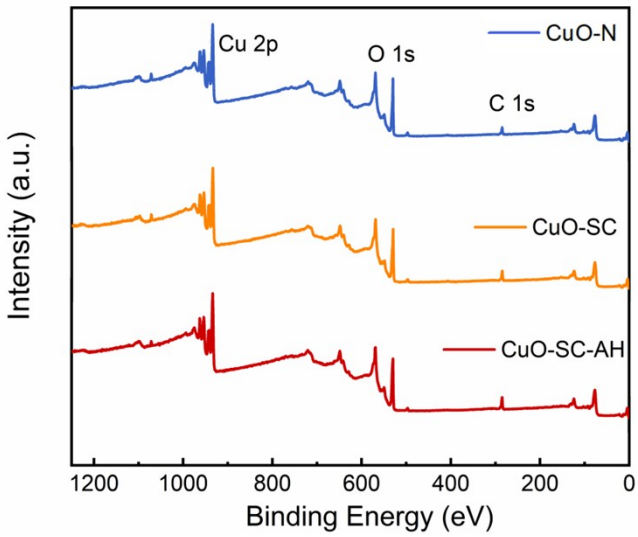

Figure S8. The XPS survey spectra of CuO, CuO-SC and CuO-SC-AH.

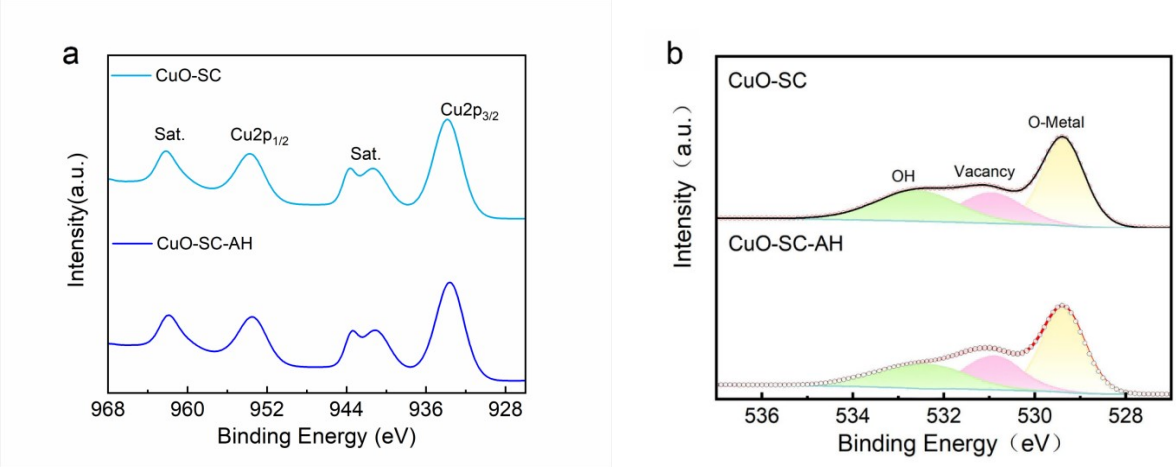

Figure S9. High-resolution XPS spectra of CuO-SC and CuO-SC-AH after the AOR test. (a) Cu 2p, (b) O 1s.

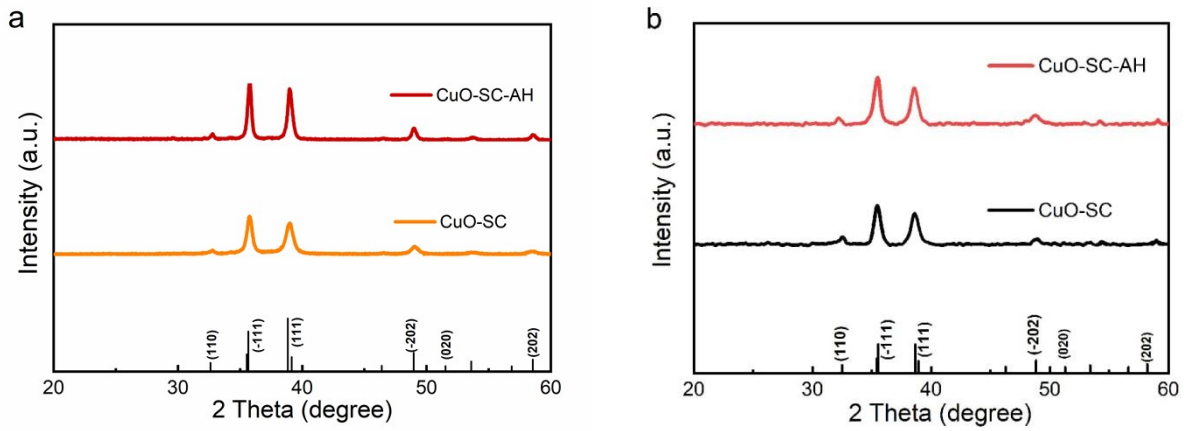

Figure S10. XRD patterns of CuO-SC and CuO-SC-AH before (a) and after (b) the AOR test.

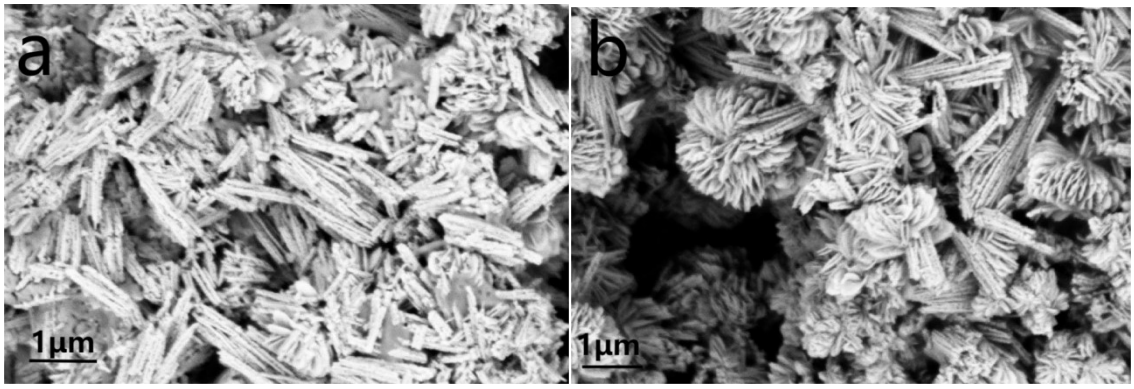

Figure S11. SEM images of CuO-SC and CuO-SC-AH after the AOR test: (a) CuO-SC, (b) CuO-SC-AH.

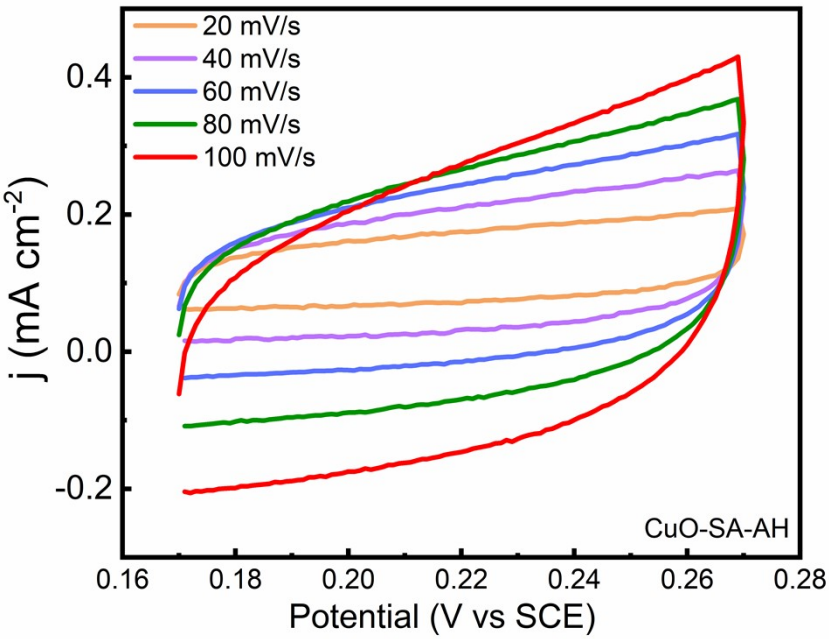

Figure S12. CV curves for CuO-SA-AH recorded in the non-Faradaic potential region at various scan rates (20 - 100 mV s^{-1}).

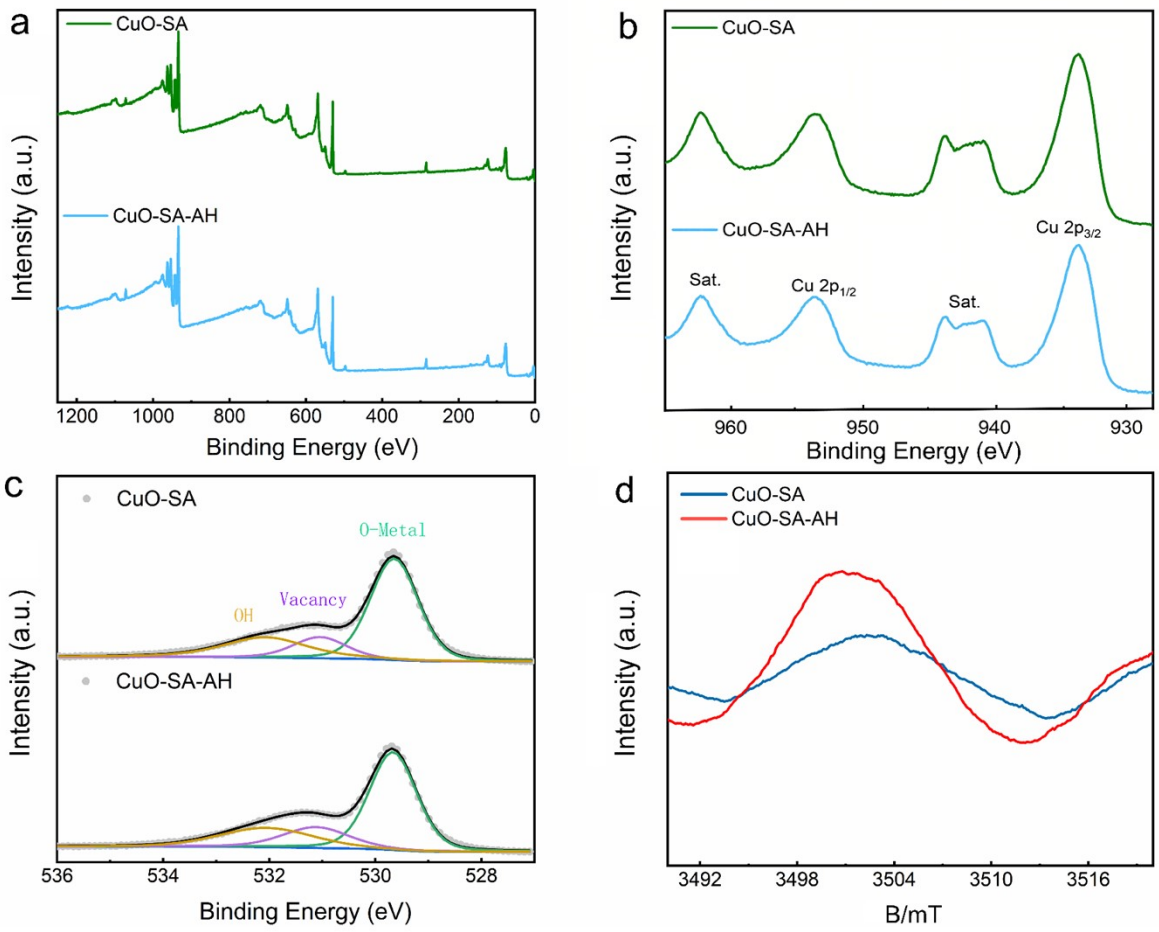

Figure S13. Comparative XPS and EPR analysis of CuO-SA and CuO-SA-AH. (a) Survey scans, (b) Cu 2p, (c) O 1s spectra, and (d) EPR spectra.

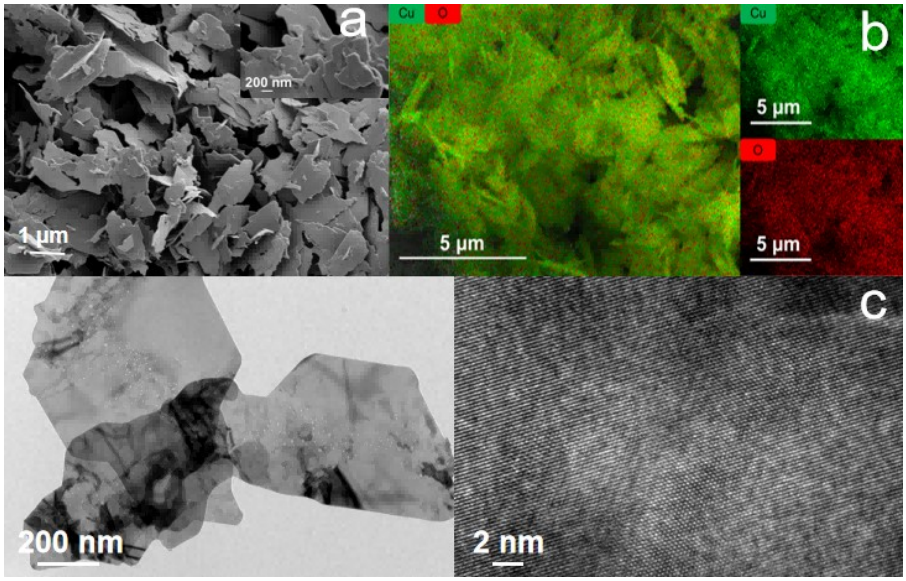

Figure S14. Microstructural and elemental characterization of CuO-SA-AH catalyst. (a) SEM image, (b) Corresponding EDS elemental mapping for Cu and O, and (c)TEM image.

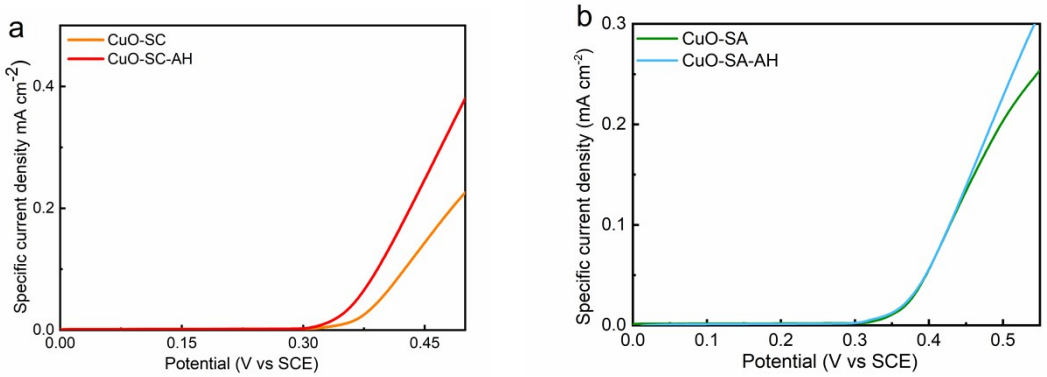

Figure S15. The ECSA-normalized polarization curves of (a) CuO-SC and CuO-SC-AH, (b) CuO-SA and CuO-SA-AH.

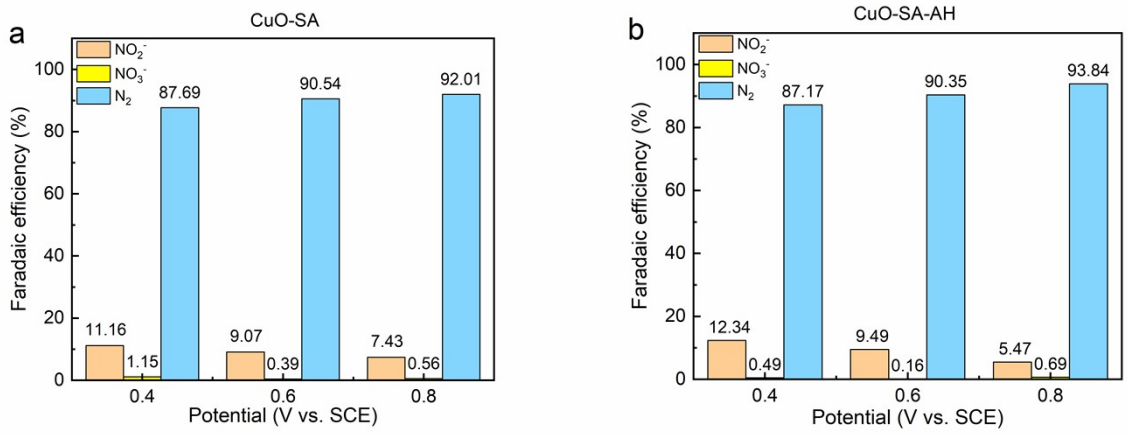

Figure S16. Potential-dependent Faradaic efficiencies (FEs) of AOR products over different catalysts. (a) CuO-SA, (b) CuO-SA-AH.